

---

# REMI: Reconstructing Episodic Memory During Intrinsic Path Planning

---

Zhaoze Wang<sup>1</sup>  
zhaoze@seas.upenn.edu

Genela Morris<sup>2,3†</sup>  
genelam@tlvmc.gov.il

Dori Derdikman<sup>4†</sup>  
derdik@technion.ac.il

Pratik Chaudhari<sup>1†</sup>  
pratikac@seas.upenn.edu

Vijay Balasubramanian<sup>5,6,7†</sup>  
vijay@physics.upenn.edu

<sup>1</sup>Department of Electrical and Systems Engineering,  
University of Pennsylvania, Philadelphia, PA 19104, USA

<sup>2</sup>Tel Aviv Sourasky Medical Center, Tel Aviv 6423906, Israel

<sup>3</sup>Gray Faculty of Medical and Health Sciences, Tel Aviv University, Tel Aviv 6997801, Israel

<sup>4</sup>Rappaport Faculty of Medicine, Technion – Israel Institute of Technology, Haifa 31096, Israel

<sup>5</sup>Department of Physics, University of Pennsylvania, Philadelphia, PA 19104, USA

<sup>6</sup>Rudolf Peierls Centre for Theoretical Physics, University of Oxford, Oxford OX1 3PU, UK

<sup>7</sup>Santa Fe Institute, Santa Fe, NM 87501, USA

<sup>†</sup>Equal contribution

## Abstract

Grid cells in the medial entorhinal cortex (MEC) are believed to path integrate speed and direction signals to activate at triangular grids of locations in an environment, thus implementing a population code for position. In parallel, place cells in the hippocampus (HC) fire at spatially confined locations, with selectivity tuned not only to allocentric position but also to environmental contexts, such as sensory cues. Although grid and place cells both encode spatial information and support memory for multiple locations, why animals maintain two such representations remains unclear. Noting that place representations seem to have other functional roles in intrinsically motivated tasks such as recalling locations from sensory cues, we propose that animals maintain grid and place representations together to support planning. Specifically, we posit that place cells auto-associate not only sensory information relayed from the MEC but also grid cell patterns, enabling recall of goal location grid patterns from sensory and motivational cues, permitting subsequent planning with only grid representations. We extend a previous theoretical framework for grid-cell-based planning and show that local transition rules can generalize to long-distance path forecasting. We further show that a planning network can sequentially update grid cell states toward the goal. During this process, intermediate grid activity can trigger place cell pattern completion, reconstructing experiences along the planned path. We demonstrate all these effects using a single-layer RNN that simultaneously models the HC-MEC loop and the planning subnetwork. We show that such recurrent mechanisms for grid cell-based planning, with goal recall driven by the place system, make several characteristic, testable predictions.

## 1 Introduction

Mammals employ various cell types to represent space and guide navigation [1–3]. For example, grid cells (GCs) in the Medial Entorhinal Cortex (MEC) fire in hexagonally arranged patterns as an animal moves through an environment [4–6]. Grid cells also exhibit multiple spatial scales in their periodic

firing patterns [7–10], which may arise through self-organization driven by inhibitory gradients in MEC attractor networks [11], enabling the efficient encoding of a large number of locations [12]. Meanwhile, hippocampal place cells (HPCs) fire at selective locations within an environment in a seemingly random manner [1, 2]. However, they are tuned not only to spatial locations but also to experiences and contextual cues [13–17]. The HPC population responses remap to form distinct representations in different environments and reinstate prior maps in familiar contexts. This ability supports their capacity to encode multiple environments without interference [2, 13, 18–20].

The local circuitry driving single GC and HPC activity has been studied extensively, and recent work shows that many of the phenomena they manifest can emerge in trained neural networks modeling their functional roles. Path integration theories propose that GCs track an animal’s position by integrating its movement, forming a continuous attractor landscape [4, 21, 22]. Likewise, recurrent neural networks (RNNs) trained to infer position from movement sequences develop grid-like patterns in their hidden layers [23–27]. For place cells, one view is that they could be emergent patterns that arise from encoding sequences of sensory signals relayed partly through the MEC [28–30] during spatial traversal [15–17, 31], perhaps implemented by a continuous attractor network (CAN) [32–35]. An alternative account is the successor representation framework [36, 37], which suggests that HPCs may encode predictive representations of future spatial states [38, 39].

Building on extensive studies of the emergence and functional roles of grid and place cells [15–17, 23, 25, 27, 40, 41], a natural view is that animals maintain these representations not just to encode space, but to support intrinsically motivated navigation tasks such as recalling goal locations from partial cues and planning paths to them. This view is supported by evidence that during rest or sleep, the hippocampus reactivates neural sequences that either mirror past paths (replay) or form novel trajectories through unvisited locations (preplay) [42, 43]. Yet, theories of place cell emergence suggest their dynamics are updated by sensory input sequences. Any planning network driving replay or preplay must therefore reproduce these inputs, or at least the sequence of sensory latent representations along the trajectory. However, if such a network could directly store and recall detailed sensory information along trajectories, the role of place cells in recall would be redundant, contradicting their well-established importance in spatial memory.

One candidate framework suggests that predictive information encoded by place cells supports transitions from the current location to neighboring states. This encoded transition likelihood traces out a most likely path connecting the current and goal locations [37]. However, this framework requires the animal to visit and encode all locations in the environment, and therefore cannot explain how animals might take shortcuts through unvisited locations. An alternative idea leverages residue number systems, enabled by multiple scales of grid cells, to encode pairwise displacements [44]. However, while grid cells can represent a vast number of locations, encoding pairwise relations among them quickly becomes intractable, fails to account for hippocampal replay and preplay, and does not explain how grid patterns would be recalled to support navigation.

Inspired by recent work suggesting that place cells may autoassociatively encode sensory inputs [16], or more generally, signals weakly modulated by space, we propose a framework unifying grid-cell-based planning with contextual recall in the hippocampus. The spatial stability of grid representations [45] allows us to treat grid cell activity as a special form of observation derived from self-motion and modulated by space. Given that the MEC, which projects to the hippocampus, contains both grid cells and neurons relaying diverse sensory signals [28–30], we propose that if place cells autoassociate both, then: (1) partial sensory input will reactivate the corresponding grid cell state through hippocampal autoassociation, enabled by recurrent connections between HC and MEC; (2) a planning network operating in grid space can use stable relative phase relationships across rooms to plan paths without rewiring when entering new environments; (3) the known local transition rules of grid cells will enable the network to construct valid paths even through unvisited areas; and (4) during planning, grid representations will advance to intermediate states, and the hippocampus will retrieve the associated sensory cues, enabling reconstruction of sensory experience along the planned trajectory.

## 2 Method

### 2.1 Hippocampus–Medial Entorhinal Cortex Loop

During spatial traversal, animals form internal representations of the world shaped by olfactory, visual, and auditory cues. These sensory signals are partially reflected by (weakly) spatially modulated cells (SMCs) in the MEC [28] and relayed to the hippocampus (HC) [46, 47]. Such observations signal the presence of, e.g., food, water, or hazards, and thus may serve not only as inputs but also as objectives for navigation. Animals also receive displacement signals from the vestibular system, proprioception, and visual flow. Although these signals may not directly correspond to specific objectives, they help animals infer their relative position from previous locations. This process is supported by grid cells (GCs) in the MEC through path integration [4, 22, 48, 49].

However, both sources of information can fail during navigation. Sensory observations may be unavailable in conditions such as dim light or nighttime, while path integration may break down due to loss or corruption of speed or direction signals. We hypothesize that animals can exploit spatial correlations between these two sources of information to achieve more accurate localization than either source alone. However, given that these correlations are context-dependent, for example varying across compartments of an enclosure or configurations of natural landmarks, this relationship is unlikely to be supported by fixed wiring between SMCs and GCs within the MEC. Instead, we propose that hippocampal place cells (HPCs) encode these correlations through pattern completion, allowing the two types of information to be flexibly wired across contexts.

With this coupling between SMCs and GCs through HPCs, animals can directly retrieve a location’s GC representation from sensory cues. The animal can then use this recalled GC representation to plan a path, as planning with GC representations is not context dependent and can therefore be generalized to any environment [44]. Along a GC-planned path, this coupling could, in turn, reconstruct SMC activity from intermediate GC states. Since GCs maintain stable relative phase relationships across environments, we further propose that planning based solely on GC representations enables shortcuts through unvisited locations and immediate planning when re-entering familiar rooms. These capabilities are not supported by HPCs alone, as they encode discrete locations and lack the continuous spatial structure required for planning. To test this proposal, we construct an RNN model of the HC-MEC loop and build a planning model on top of it.

#### 2.1.1 A RNN Model of the HC-MEC Loop

**Integrate input and output cells directly into recurrent dynamics.** Previous RNN models characterizing emergence of GCs and HPCs [16, 23, 25, 27, 50] have a limitation for planning: they typically do not explicitly model signals driving recurrent dynamics but instead rely on a learnable projection matrix. We posit that, during planning, these signals serve as control inputs to drive the HC-MEC loop toward the goal (see Sec. 4). Explicitly modeling these inputs simplifies the architecture and enables joint modeling of HC, MEC, and the planning subnetwork within a single recurrent structure.

Consider a standard RNN used in previous studies [16, 23, 25, 27, 50], updating its dynamics as:

$$z_{t+1} = \alpha \cdot z_t + (1 - \alpha) \cdot (\mathbf{W}^{in} u_t + \mathbf{W}^{rec} f(z_{t-1})) \quad (1)$$

where  $z \in \mathbb{R}^{d_z}$  is the hidden state,  $u$  is the input,  $\alpha$  is the forgetting rate, and  $\mathbf{W}^{in}$ ,  $\mathbf{W}^{rec}$  are the input and recurrent weight matrices. The output is given by a linear readout:  $y_t = \mathbf{W}^{out} z_t \in \mathbb{R}^{d_o}$ . We extend this RNN by introducing auxiliary input and output nodes,  $z^I$  and  $z^O$ , and update as:

$$\begin{bmatrix} z_{t+1} \\ z_{t+1}^I \\ z_{t+1}^O \end{bmatrix} = \alpha \odot \begin{bmatrix} z_t \\ z_t^I \\ z_t^O \end{bmatrix} + (1 - \alpha) \odot \left( \begin{bmatrix} \mathbf{0} \\ u_t \\ \mathbf{0} \end{bmatrix} + \begin{bmatrix} \mathbf{W}^{rec} & \tilde{\mathbf{W}}^{in} & \mathbf{W}^{(13)} \\ \mathbf{W}^{(21)} & \mathbf{W}^{(22)} & \mathbf{W}^{(23)} \\ \tilde{\mathbf{W}}^{out} & \mathbf{W}^{(32)} & \mathbf{W}^{(33)} \end{bmatrix} f \left( \begin{bmatrix} z_t \\ z_t^I \\ z_t^O \end{bmatrix} \right) \right) \quad (2)$$

Here,  $z^I$  directly integrates the input  $u_t$  without a learnable projection, while  $z^O$  is probed and supervised to match simulated ground-truth cell responses. This design eliminates the need for projection matrices  $\mathbf{W}^{in}$  and  $\mathbf{W}^{out}$ . Instead,  $\tilde{\mathbf{W}}^{in}$  and  $\tilde{\mathbf{W}}^{out}$  act as surrogate mappings for the original projections. We set  $\alpha$  as a learnable vector in  $\mathbb{R}^{d_z+d_I+d_O}$  to allow different cells to have distinct forgetting rates, with  $\odot$  denoting element-wise multiplication.

We assign speed cells and allocentric direction cells as input nodes that only receive inputs. The SMCs are set to both input and output nodes, trained to match the simulated ground truth. These SMCs

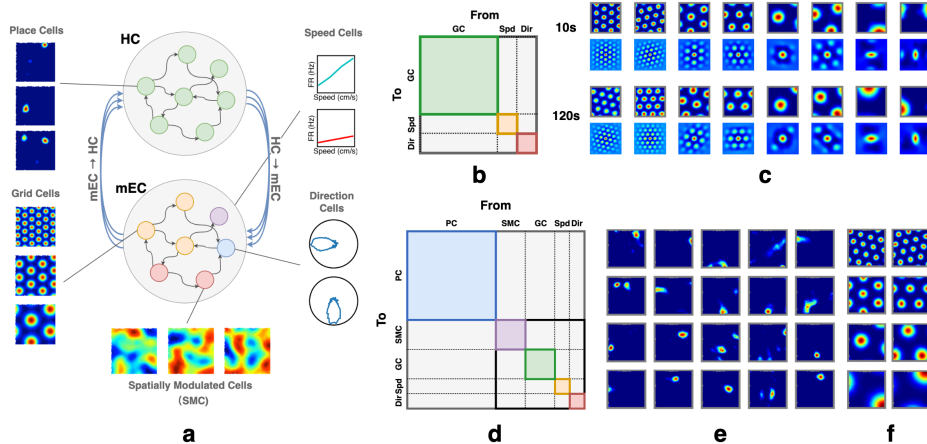


**Figure 1:** (a) RNN model of the HC-MEC loop. The top subnetwork contains HPCs, with example emergent place fields shown on the left. The bottom subnetwork includes partially supervised GCs, as well as supervised speed, direction, and spatially modulated cells (SMCs); example grid fields shown at left. (b) & (d) Speed cells and direction cells are denoted as *Spd* and *Dir*, respectively. Colored regions highlight within-group recurrent connectivity to indicate the partitioning of the connectivity matrix by cell groups. However, at initialization, no structural constraints are enforced. The full connectivity matrix is randomly initialized. (b) Illustration of the path-integration network’s connectivity matrix. (c) The network is trained to path-integrate 5s trials and tested on 10s trials ( $L = 100.50 \pm 8.49$  cm); the grid fields remain stable even in trials up to 120s ( $L = 1207.89 \pm 30.98$  cm). For each subpanel (10s, 120s): top row shows firing fields; bottom row shows corresponding autocorrelograms. (d) Illustration of RNN connectivity matrix of full HC-MEC loop. (e-f) Example place fields (emergent) and grid fields in the full HC-MEC RNN model.

are assumed to primarily respond to sensory cues during physical traversal. Supervision constrains their dynamics to reflect tuning to these signals, while learned recurrent connections formed during training are intended to reflect Hebb-like updates in brain that preserve this tuning structure. The ground truth signals for all cells are strictly positive to reflect firing rates (see Suppl. 3 for how ground truth signals are simulated). For direction cells, we assign allocentric preferred directions uniformly over  $[0, 2\pi)$  with a fixed angular tuning width, ensuring their responses remain non-negative and their population activity lies on a 1D ring.

**Partially Supervise Grid Cells.** For our proposed planning mechanism, we must model a complete HC-MEC loop containing stable patterns of both GCs and HPCs. However, no existing model exhibits the simultaneous emergence of grid and place cells. To address this, we supervise GCs to learn path integration. Specifically, we simulate GC population responses within a room and use them as ground truth. At the start of each training trajectory, RNN hidden units modeling grid cells are initialized to the ground-truth GC responses at the starting location. Along this trajectory, the network receives only speed and direction signals, directly input to the corresponding cells and relayed to the GC subpopulation through recurrent projections. We collect GC subpopulation states over time and penalize their deviation from simulated ground-truth responses, encouraging controllable GC activity while learning path integration. We refer to this as *partial supervision* and apply it to GCs for three reasons: (1) our primary focus is to test planning by the HC-MEC loop rather than the co-emergence of both GCs and HPCs; (2) HPC remapping in novel environments involves extensive reorganization of spatial tuning and synaptic connections driven by sensory input [40, 51, 52], making it harder to parameterize and simulate than GCs, which exhibit greater stability [45] and maintain stable relative phase relationships across environments [3, 53]; (3) the planning mechanism critically depends on the experimentally established stability of GC phase relationships and multiple spatial scales, as we will show in the following sections; these properties are difficult to control in existing emergence models.

We recognize that, biologically, HPCs appear before grid cells (GCs) [3, 54–56]; however, HPC firing fields become more spatially precise as GCs mature, suggesting an iterative refinement process [56, 57]. Conceptually, our HC-MEC model with partially supervised GCs can be seen as capturing this refinement phase, where the emergence of GCs enhances the spatial specificity of HPCs. Reflecting

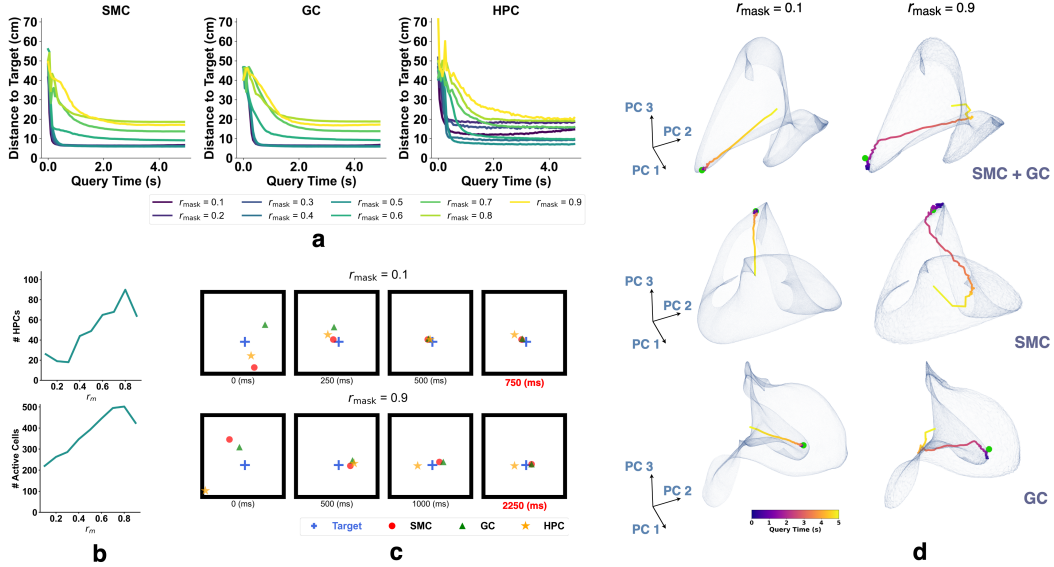


**Figure 2:** Recalling MEC representations from sensory observations with networks trained under different masking ratios  $r_{\text{mask}}$ . **(a–d)** Results from querying the trained network with fixed sensory input. **(a)** L2 distance between decoded and target positions using SMCs, GCs, and HPCs. **(b)** Top: number of identified HPCs vs.  $r_{\text{mask}}$  (max 512). Bottom: number of active hippocampal units vs.  $r_{\text{mask}}$  (max 512). **(c)** Decoded positions from SMC, GC, and HPC population responses. **(d)** Example recall trajectories for SMC, GC, and their concatenation. Semi-transparent surfaces show PCA-reduced ratemaps (extrapolated 5 $\times$  for visualization) from testing. Trajectories are colored by time; green dot marks the target.

this process, we observe a quick emergence during early training and a corresponding reduction in HPC firing field widths after GCs are learned (see Suppl. 5.1).

**Testing GC Path Integration and HPC Emergence.** Planning requires stable GC and/or PC representations. Before discussing planning, we first train the network to develop these representations. We first test whether a GC network trained with partial supervision can perform path integration. We simulate six modules with spatial periodicities scaled by the theoretical optimal factor  $\sqrt{e}$  [12]. The smallest grid spacing is set to 30 cm, defined as the distance between two firing centers of a grid cell [58]. The grid spacing to field size ratio is 3.26 [59], with firing fields modeled as Gaussian blobs with radii equal to two standard deviations. We train this model on short random trajectories (5 s) but accurately path-integrate over significantly longer trajectories (10 s, 120 s) during testing (Figure 1c).

We then test the full HC-MEC loop model. Both supervised and partially supervised cells receive masked input and initial states, with supervised cells additionally receiving inputs at all timesteps. The HPC subnetwork receives signals only from MEC through recurrent connections and does not take external input. All cells are modeled within a single recurrent network without explicit connectivity constraints (see Figure 1d for initialization details). We observe HPCs emerge in the network, while GCs learn to path integrate (Figure 1e-f).

### 3 Recalling MEC Representations from Sensory Observations

We first tested that sensory observations at the goal location can trigger retrieval of the corresponding grid cell (GC) representation through auto-association of GCs and spatially modulated cells (SMCs). Auto-association is expected to occur when the input pattern is incomplete or degraded. To evaluate this, we trained nine models with identical configurations, varying only the masking ratio  $r_{\text{mask}}$  from 0.1 to 0.9. The masking ratio  $r_{\text{mask}}$  specifies the maximum fraction of direction, speed, GC, and SMC inputs, as well as their initial hidden states, that are randomly set to zero during training. This simulates degraded observations and encourages the network to learn robust recall through auto-association. Each model was trained on randomly sampled short trajectories using a fixed  $r_{\text{mask}}$ ,



with new random masks generated for every trajectory and varying across time and cells. Masks were applied to both the inputs and initial states of GCs, SMCs, speed cells, and direction cells (Suppl. 5.2).

After training, we randomly selected locations in the environment and sampled the corresponding ground-truth SMC responses. Each sampled response was repeated  $T$  times to form a query. During queries, the network state was initialized to zero across all hidden-layer neurons, and the query was input only to the spatial modulated cells, while responses from all cells were recorded over  $T$  timesteps. At each timestep, the activity of a subpopulation of cells (e.g., SMC, GC, HPC) was decoded into a position by finding the nearest neighbor on the corresponding subpopulation ratemap aggregated during testing (Suppl.5.4). Nearest neighbor search was performed using FAISS [60, 61] (Suppl.4).

Figure 2a shows the L2 distance between decoded and ground-truth positions over time. The network was queried for 5 seconds (100 timesteps), and all models successfully recalled the goal location with high accuracy. HPCs were identified as neurons with mean firing rates above 0.01 Hz and spatial information content (SIC) above 20 (Suppl. 2.1). The number of HPCs increased with  $r_{\text{mask}}$ , and location decoding using HPCs was performed only for models with more than 10 HPCs. We observe a trade-off in which higher  $r_{\text{mask}}$  leads to more HPCs and improved decoding accuracy but reduces the network’s ability to recall sensory observations (Figure 2a,b).

To visualize the recall process (Figure 2c), we conducted Principal Components Analysis (PCA) on the recall trajectories. We first flattened the  $L_x \times L_y \times N$  ground-truth ratemap into a  $(L_x \cdot L_y) \times N$  matrix, where  $L_x$  and  $L_y$  are the spatial dimensions of the arena and  $N$  is the number of cells in each subpopulation. PCA was then applied to reduce this matrix to  $(L_x \cdot L_y) \times 3$ , retaining only the first three principal components. The trajectories (colored by time), goal responses (green dot), and ratemaps collected during testing were projected into this reduced space for visualization. In Figure 2d, the recall trajectories for all subpopulations converge near the target representation, indicating successful retrieval of target SMC and GC patterns. Once near the target, the trajectories remain close and continue to circulate around it, indicating stable dynamics during the recall process.

## 4 Planning with Recalled Representations

The recall experiment above demonstrates that auto-association of spatially modulated cells (SMCs) and grid cells (GCs) through hippocampal place cells (HPCs) could enable the recall of all cells’ (GC, HPC, and SMC) representations using sensory cues. Among the recalled patterns, we propose that animals primarily use GCs for planning, as direct planning with HPCs or SMCs cannot take shortcut paths through unvisited regions. Auto-association removes the need for direct planning with SMCs or HPCs; sensory cues are required only to determine initial and target GC representations. Once recalled, a sequence of speed and direction signals drives GC activity from the initial to the target pattern, generating the planned path. Sensory patterns can then be reconstructed from intermediate GC states through HPCs, further reducing reliance on SMCs and HPCs during planning. These speed and direction signals are context-free and generalizable across environments, allowing planning strategies learned in one room to transfer to others. Finally, planning within GC representations may enable local transition rules to generalize to long-range path planning.

### 4.1 Decoding Displacement from Grid Cells

We first revisit and reframe the formalism in [44]. Grid cells are grouped into modules based on shared spatial periods and orientations. Within each module, relative phase relationships remain stable across environments [10, 58, 62, 63]. This stability allows the population response of a grid module to be represented by a single phase variable  $\phi$  [44], which is a scalar in 1D and a 2D vector in 2D environments. This variable maps the population response onto an  $n$ -dimensional torus [64], denoted as  $\mathbb{T}^n = \mathbb{R}^n / 2\pi\mathbb{Z}^n \cong [0, 2\pi)^n$ , where  $n \in \{1, 2\}$  is the dimension of navigable space.

Consider a 1D case with  $\phi_c$  and  $\phi_t$  as the phase variables of the current and target locations in some module. The phase difference is  $\Delta\phi = \phi_t - \phi_c$ , and since  $\phi_c, \phi_t \in [0, 2\pi)$ , we have  $\Delta\phi \in (-2\pi, 2\pi)$ . However, for vector-based navigation, we instead need  $\Delta\phi^*$  such that  $\phi_t = [\phi_c + \Delta\phi^*]_{2\pi}$ , where  $[\cdot]_{2\pi}$  is an element-wise modulo operation so that  $\phi_t$  is defined on  $[0, 2\pi)$ . Simply using  $\Delta\phi$  directly is not sufficient because multiple wrapped phase differences correspond to the same phase  $\phi_t$ , but different physical positions on the torus. Therefore, we restrict  $\Delta\phi$  to be defined on  $(-\pi, \pi)$  such that

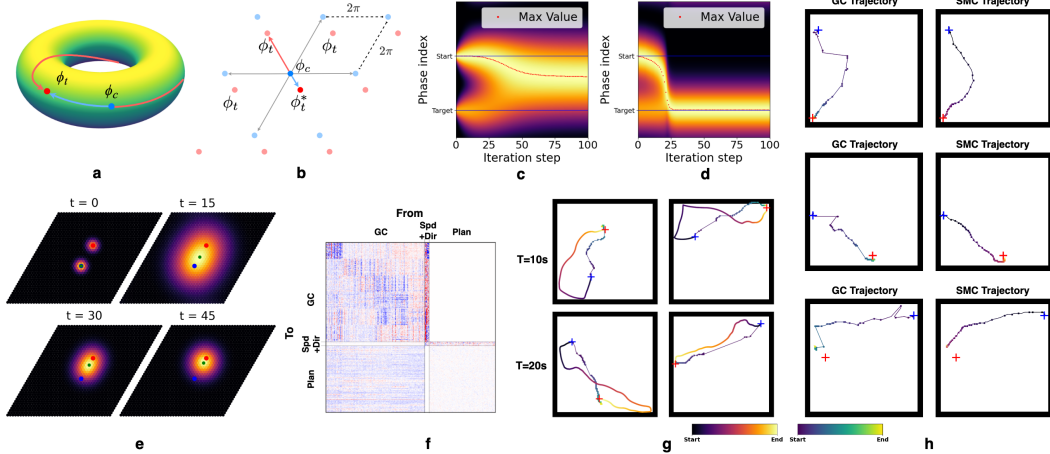


**Figure 3:** (a) The population response of a single grid module forms an  $n$ -dimensional torus, where multiple phase differences can connect the current and target phases. (b) Unwrapping phases into physical space yields  $2^n$  candidate displacements; only  $\phi_t^*$  lies within the principal domain  $(-\pi, \pi)^n$ . (c) A Markovian process asymptotically identifies the most likely next phase that moves closer to the target. (d) Renormalizing after each update produces a smooth trajectory from start to target. (e) Illustration of this process in 2D space. (f) Learned connectivity matrix of the planning RNN using only grid cells. (g) Planned trajectories for targets reachable within 10 and 20 seconds. Blue and red crosses mark start and target locations; the reference line shows the full trajectory for visualization. The dots represented the decoded locations. (h) A planning network connected to the full HC-MEC, receiving input only from GC and controlling speed and direction, drives SMC responses to update alongside GC, tracing a trajectory closely aligned with the planned GC path.

the planning mechanism always selects the shortest path on the torus that points to the target phase. The decoded displacement in physical space is then  $\hat{d} \in [-\ell/2, \ell/2]$ .

For 2D space, we define  $\Delta\phi \in \mathbb{R}^2$  on  $(-\pi, \pi)^2$  by treating the two non-collinear directions as independent 1D cases. In Figure 3a, the phase variables  $\phi_c$  and  $\phi_t$  correspond to two points on a 2D torus. When unwrapped into physical space, these points repeat periodically, forming an infinite lattice of candidate displacements (Figure 3b). In 2D, this yields four ( $2^2$ ) distinct relative positions differing by integer multiples of  $2\pi$  in phase space. Only the point  $\phi_t^*$  lies within the principal domain  $(-\pi, \pi)^2$ , and the decoder selects  $\Delta\phi \in (-\pi, \pi)^2$  that minimizes  $\|\Delta\phi\|$ , subject to  $\phi_t = [\phi_c + \Delta\phi]_{2\pi}$ .

## 4.2 Sequential Planning

Previous network models compute displacement vectors from GCs by directly decoding from the current  $\phi_c$  and the target  $\phi_t$  [44]. However, studies show that during quiescence, GCs often fire in coordinated sequences tracing out trajectories [65, 66], rather than representing single, abrupt movements toward the target. At a minimum, long-distance displacements are not directly executable and must be broken into smaller steps. What mechanism could support such sequential planning?

We first consider a simplistic planning model on a single grid module. Phase space can be discretized into  $N_\phi$  bins, grouping GC responses into  $N_\phi$  discrete states. Local transition rules can be learned even during random exploration, allowing the animal to encode transition probabilities between neighboring locations. These transitions can be compactly represented by a matrix  $T \in \mathbb{R}^{N_\phi \times N_\phi}$ , where  $T_{ij}$  gives the probability of transitioning from phase  $i$  to phase  $j$ . With this transition matrix, the animal can navigate to the target by stitching together local transitions, even without knowing long-range displacements. Specifically, suppose we construct a vector  $v^{\text{plan}} \in \mathbb{R}^{N_\phi}$  with nonzero entries marking the current and target phases to represent a planning task. Multiplying  $v^{\text{plan}}$  by matrix  $T$  propagates the current and target phases to their neighboring phases, effectively performing a “search” over possible next steps based on known transitions.

By repeatedly applying this update, the influence of the current and target phase spreads through phase space, eventually settling on an intermediate phase that connects start and target (Figure 3c). If

the animal selects the phase with the highest value after each update and renormalizes the vector, this process traces a smooth trajectory toward the target (Figure 3d). This approach can be generalized to 2D phase spaces (Figure 3e). In essence, we propose that the animal can decompose long-range planning into a sequence of local steps by encoding a transition probability over phases in a matrix. A readout mechanism can then map these phase transitions into corresponding speeds and directions and subsequently update GC activity toward the target. We also note that this iterative planning process resembles search-based methods in robotics, such as RRT-Connect [67].

### 4.3 Combining Decoded Displacement from Multiple Scales

Our discussions of planning and decoding in sections 4.1 and 4.2 were limited to displacements within a single grid module. However, this is insufficient when  $\Delta\phi$  exceeds half the module’s spatial period ( $\ell/2$ ). The authors of [44] proposed combining  $\Delta\phi$  across modules before decoding displacement. We instead suggest decoding  $\Delta\phi$  within each module first, then averaging the decoded displacements across modules is sufficient for planning. This procedure allows each module to update its phase using only local transition rules while still enabling the animal to plan a complete path to the target.

We start again with the 1D case. Suppose there are  $m$  different scales of grid cells, with each scale  $i$  having a spatial period  $\ell_i$ . From the smallest to the largest scale, these spatial periods are  $\ell_1, \dots, \ell_m$ . The grid modules follow a fixed scaling factor  $s$ , which has a theoretically optimal value of  $s = e$  in 1D rooms and  $s = \sqrt{e}$  in 2D [12]. Thus, the spatial periods satisfy  $\ell_i = \ell_0 \cdot s^i$  for  $i = 1, \dots, m$ , where  $\ell_0$  is a constant parameter that does not correspond to an actual grid module.

Given the ongoing debate about whether grid cells contribute to long-range planning [68, 69], we focus on mid-range planning, where distances are of the same order of magnitude as the environment size. Suppose two locations in 1D space are separated by a ground truth displacement  $d \in \mathbb{R}_+$ , bounded by half the largest scale ( $\ell_m/2$ ). We can always find an index  $k$  where  $\ell_1/2, \dots, \ell_k/2 \leq d < \ell_{k+1}/2 < \dots, \ell_m/2$ . Given  $k$ , we call scales  $\ell_{k+1}, \dots, \ell_m$  **decodable** and scales  $\ell_1, \dots, \ell_k$  **undercovered**. For undercovered scales, phase differences  $\Delta\phi$  are wrapped around the torus at least one period of  $(-\pi, \pi)$  and may point to the wrong direction. We thus denote phase difference from undercovered scales as  $Z_i$ . If we predict displacement by simply averaging the decoded displacements from all grid scales, the predicted displacement is:

$$\hat{d} = \frac{\ell_0}{2\pi m} \cdot \left( \sum_{i=1}^k s^i \cdot Z_i + \sum_{i=k+1}^m s^i \cdot \Delta\phi_i \right)$$

In 1D, the remaining distance after taking the predicted displacement is  $d_{\text{next}} = d_{\text{current}} - \hat{d}$ . For the predicted displacement to always move the animal closer to the target, meaning  $d_{\text{next}} < d_{\text{current}}$ , it suffices that  $m > k + \frac{1-s^{-k}}{s-1}$  (see Suppl. 1.1). This condition is trivially satisfied in 1D for  $s = e$ , as  $\frac{1-s^{-k}}{s-1} < 1$  requiring only  $m > k$ . In 2D, where the optimal scaling factor  $s = \sqrt{e}$ , the condition tightens slightly to  $m > k + 1$ . Importantly, as the animal moves closer to the target, more scales become decodable, enabling increasingly accurate predictions that eventually lead to the target. In 2D, planning can be decomposed into two independent processes along non-collinear directions. Although prediction errors in 2D may lead to a suboptimal path, this deviation can be reduced by increasing the number of scales or taking smaller steps along the decoded direction, allowing the animal to gradually approach the target with higher prediction accuracy.

### 4.4 A RNN Model of Planning

**Planning Using Grid Cells Only.** We test our ideas in an RNN framework. We first ask whether a planner subnetwork, modeled together with a GC subnetwork, can generate sequential trajectories toward the target using only grid cell representations. Accordingly, we connect a planning network to a pre-trained GC network that has already learned path integration. For each planning task, the GC subnetwork is initialized with the ground truth GC response at the start location, while the planner updates the GC state from the start to the target location’s GC response by producing a sequence of feasible actions—specifically, speeds and directions. This ensures the planner generates feasible actions rather than directly imposing the target state on the GCs, while a projection from the GC region to the planning region keeps the planner informed of the current GC state. The planner additionally receives the ground truth GC response of the target location through a learnable linear projection. At each step, the planner receives  $\mathbf{W}^{in} g^* + \mathbf{W}^{g \rightarrow p} g_t \in \mathbb{R}^{d_p}$ , where  $g^*$  and  $g_t$  are the



goal and current GC patterns, while  $\mathbf{W}^{in}$  and  $\mathbf{W}^{g \rightarrow p}$  are the input and GC-to-planner projection matrices. This combined input has the same dimension as the planner network. Conceptually, it can be interpreted as the planning vector  $v^{plan}$ , while the planner’s recurrent matrix represents the transition matrix  $T$ . The resulting connectivity matrix is shown in Figure 3f.

During training, we generate random 1-second trajectories to sample pairs of current and target locations, allowing the animal to learn local transition rules. These trajectories are used only to ensure that the target location is reachable within 1 second from the current location; the trajectories themselves are not provided to the planning subnetwork. The planning subnetwork is trained to minimize the mean squared error between the current and target GC states for all timesteps.

For testing, we generate longer 10 and 20 second trajectories to define start and target locations, again without providing the full trajectories to the planner. The GC states produced during planning are decoded at each step to infer the locations the animal is virtually planned to reach. As shown in Figure 3g, the dots represent these decoded locations along the planned path, while the colored line shows the full generated trajectory for visualization and comparison. We observe that the planner generalizes from local to long-range planning and can take paths that shortcut the trajectories used to generate start and target locations. Notably, even when trained on just 128 fixed start-end pairs over 100 steps, it still successfully plans paths between locations reachable over 10 seconds.

***Planning with HC-MEC Enables Reconstruction of Sensory Experiences Along Planned Paths.***

We next test whether the HC-MEC loop enables the network to reconstruct sensory experiences along planned trajectories using intermediate GC states. To this end, we connect an untrained planning subnetwork to a pre-trained HC-MEC model ( $r_{mask} = 1.0$ , see Suppl. 5.2) and fix all projections from SMCs and HPCs to the planner to zero. This ensures the planner uses only GC representations for planning and controls HC-MEC dynamics by producing inputs to speed and direction cells. SMCs and GCs are initialized to their respective ground truth responses at the start location.

Using the same testing procedures as before, we sampled the SMC and GC responses while the planner generated paths between two locations reachable within 10 seconds. We decoded GC and SMC activity at each timestep to locations using nearest neighbor search on their respective ratemaps. We found that the decoded SMC trajectories closely followed those of the GCs, suggesting that SMC responses can be reconstructed from intermediate GC states via HPCs (see Figure 3h). Additionally, compared to the GC-only planning case, we reduced the number of GCs in the HC-MEC model to avoid an overly large network, which would make the HC-MEC training hard to converge. Although this resulted in a less smooth GC-decoded trajectory than in Figure 3g, the trajectory decoded from SMCs was noticeably smoother. We suggest this is due to the auto-associative role of HPCs, which use relayed GC responses to reconstruct SMCs, effectively smoothing the trajectory.

## 5 Discussion

Decades of theoretical and computational research have sought to explain how and why hippocampal place cells (HPCs) and grid cells (GCs) emerge. These models address the question “What do they encode?” But an equally important question is “Why does the brain encode?” One answer is that animals develop and maintain place and grid representations to support intrinsically motivated navigation, enabling access to resources critical to survival, such as food, water, and shelter. Thus, we take the perspective: *given the known phenomenology of GCs and HPCs, how might they be wired together to support intrinsically motivated navigation?*

Previous studies show that HPCs are linked to memory and context but have localized spatial representations lacking the relational structure needed for planning. In contrast, the periodic lattice of GCs supports path planning by generalizing across environments, but weak contextual tuning limits direct recall of GC patterns from sensory cues. Rather than viewing GCs and HPCs as parallel spatial representations, we propose that GCs and spatially modulated cells (SMCs), reflecting sensory observations, form parallel, independent localization systems, each encoding different aspects of space. HPCs then link these representations through auto-association, enabling recovery of one when the other fails and providing a higher-level, abstract spatial representation.

Testing these ideas, we built a single-layer RNN that simultaneously models GCs, HPCs, SMCs, and a planning subnetwork. We showed that auto-association in HPCs, linking MEC sensory (SMCs) and spatial (GCs) representations enables recall of GC patterns from contextual cues. With recalled

GC patterns, local planning using only GCs can be learned and generalized to longer trajectories. Finally, HPCs can reconstruct sensory experiences along planned paths, obviating the need for direct planning based solely on HPCs or SMCs. Our model is flexible and accommodates existing theories, as follows. Recurrent connections from MEC cause HPC activity to lag one timestep behind MEC inputs; during pattern completion, HPCs implicitly learn to predict the next timestep’s MEC inputs, and thus can account for the successor representation theory of HPCs [36]. This predictive nature is thus consistent with previous theories that predictive coding in HPCs could support planning [37], but we emphasize that using GCs may be more efficient when it is necessary to shortcut unvisited locations. Lastly, while we propose that the HC–MEC coupling enables planning through recall and reconstruction, a parallel idea was proposed in [70], where the same coupling was argued to support increased episodic memory capacity.

Our theory makes several testable predictions. First, sensory cues should reactivate GC activity associated with a target location, even when the animal is stationary or in a different environment. Second, inhibiting MEC activity should impair path planning and disrupt sequential preplay in the HC. Finally, if hippocampal place cells reconstruct sensory experiences during planning, disrupting MEC-to-HC projections should impair goal-directed navigation, while disrupting HC-to-MEC feedback should reduce planning accuracy by preventing animals from validating planned trajectories internally.

**Limitations:** First, existing emergence models of GCs make it difficult to precisely control GC scales and orientations [11, 26], and so to avoid the complicating analysis of the simultaneous emergence of GCs and HPCs, we supervised GC responses during training. Future work on their co-emergence could further support our proposed planning mechanism. Second, our framework does not account for boundary avoidance, which would require extending the HC-MEC model to include boundary cell representations [40, 71, 72]. Finally, our discussion of planning with GCs assumes the environment is of similar scale to the largest grid scale. One possibility is long-range planning may involve other brain regions [69], as suggested by observations that bats exhibit only local 3D grid lattices without a global structure [68]. Animals might use GCs for mid-range navigation, while global planning stitches together local displacement maps from GC activity.

## Acknowledgments and Disclosure of Funding

The study was supported by NIH CRCNS grant 1R01MH125544-01 and in part by the NSF and DoD OUSD (R&E) under Agreement PHY-2229929 (The NSF AI Institute for Artificial and Natural Intelligence). Additional support was provided by the United States–Israel Binational Science Foundation (BSF). PC was supported in part by grants from the National Science Foundation (IIS-2145164, CCF-2212519) and the Office of Naval Research (N00014-22-1-2255). VB was supported in part by the Eastman Professorship at Balliol College, Oxford.

## References

- [1] Edvard I. Moser, Emilio Kropff, and May-Britt Moser. Place Cells, Grid Cells, and the Brain’s Spatial Representation System. *Annual Review of Neuroscience*, 31(1):69–89, July 2008.
- [2] May-Britt Moser, David C. Rowland, and Edvard I. Moser. Place Cells, Grid Cells, and Memory. *Cold Spring Harbor Perspectives in Biology*, 7(2):a021808, February 2015.
- [3] Genela Morris and Dori Derdikman. The chicken and egg problem of grid cells and place cells. *Trends in Cognitive Sciences*, 27(2):125–138, February 2023.
- [4] Torkel Hafting, Marianne Fyhn, Sturla Molden, May-Britt Moser, and Edvard I. Moser. Microstructure of a spatial map in the entorhinal cortex. *Nature*, 436(7052):801–806, August 2005.
- [5] David C. Rowland, Yasser Roudi, May-Britt Moser, and Edvard I. Moser. Ten Years of Grid Cells. *Annual Review of Neuroscience*, 39(1):19–40, July 2016.
- [6] Edvard I Moser, May-Britt Moser, and Bruce L McNaughton. Spatial representation in the hippocampal formation: A history. *Nature Neuroscience*, 20(11):1448–1464, November 2017.
- [7] Caswell Barry, Robin Hayman, Neil Burgess, and Kathryn J Jeffery. Experience-dependent rescaling of entorhinal grids. *Nature Neuroscience*, 10(6):682–684, June 2007.
- [8] Vegard Heimly Brun, Trygve Solstad, Kirsten Brun Kjelstrup, Marianne Fyhn, Menno P. Witter, Edvard I. Moser, and May-Britt Moser. Progressive increase in grid scale from dorsal to ventral medial entorhinal cortex. *Hippocampus*, 18(12):1200–1212, December 2008.
- [9] Hanne Stensola, Tor Stensola, Trygve Solstad, Kristian Frøland, May-Britt Moser, and Edvard I. Moser. The entorhinal grid map is discretized. *Nature*, 492(7427):72–78, December 2012.
- [10] Julija Krupic, Marius Bauza, Stephen Burton, Caswell Barry, and John O’Keefe. Grid cell symmetry is shaped by environmental geometry. *Nature*, 518(7538):232–235, February 2015.
- [11] Louis Kang and Vijay Balasubramanian. A geometric attractor mechanism for self- organization of entorhinal grid modules. *eLife*, 8, August 2019.
- [12] Xue-Xin Wei, Jason Prentice, and Vijay Balasubramanian. A principle of economy predicts the functional architecture of grid cells. *eLife*, 4:e08362, September 2015.
- [13] Charlotte B. Alme, Chenglin Miao, Karel Jezek, Alessandro Treves, Edvard I. Moser, and May-Britt Moser. Place cells in the hippocampus: Eleven maps for eleven rooms. *Proceedings of the National Academy of Sciences*, 111(52):18428–18435, December 2014.
- [14] John L. Kubie, Elliott R. J. Levy, and André A. Fenton. Is hippocampal remapping the physiological basis for context? *Hippocampus*, 30(8):851–864, August 2020.
- [15] Marcus K. Benna and Stefano Fusi. Place cells may simply be memory cells: Memory compression leads to spatial tuning and history dependence. *Proceedings of the National Academy of Sciences*, 118(51):e2018422118, December 2021.
- [16] Zhaoze Wang, Ronald W. Di Tullio, Spencer Rooke, and Vijay Balasubramanian. Time Makes Space: Emergence of Place Fields in Networks Encoding Temporally Continuous Sensory Experiences. In *NeurIPS 2024*, August 2024.
- [17] Markus Pettersen and Frederik Rogge. Learning Place Cell Representations and Context-Dependent Remapping. *38th Conference on Neural Information Processing Systems (NeurIPS 2024)*, September 2024.
- [18] R. Monasson and S. Rosay. Transitions between Spatial Attractors in Place-Cell Models. *Physical Review Letters*, 115(9):098101, August 2015.
- [19] Aldo Battista and Rémi Monasson. Capacity-Resolution Trade-Off in the Optimal Learning of Multiple Low-Dimensional Manifolds by Attractor Neural Networks. *Physical Review Letters*, 124(4):048302, January 2020.
- [20] Spencer Rooke, Zhaoze Wang, Ronald W. Di Tullio, and Vijay Balasubramanian. Trading Place for Space: Increasing Location Resolution Reduces Contextual Capacity in Hippocampal Codes. In *NeurIPS 2024*, October 2024.
- [21] Mark C. Fuhs and David S. Touretzky. A Spin Glass Model of Path Integration in Rat Medial Entorhinal Cortex. *The Journal of Neuroscience*, 26(16):4266–4276, April 2006.

- [22] Yoram Burak and Ila R. Fiete. Accurate Path Integration in Continuous Attractor Network Models of Grid Cells. *PLoS Computational Biology*, 5(2):e1000291, February 2009.
- [23] Christopher J. Cueva and Xue-Xin Wei. Emergence of grid-like representations by training recurrent neural networks to perform spatial localization, March 2018.
- [24] Andrea Banino, Caswell Barry, Benigno Uribe, Charles Blundell, Timothy Lillicrap, Piotr Mirowski, Alexander Pritzel, Martin J. Chadwick, Thomas Degris, Joseph Modayil, Greg Wayne, Hubert Soyer, Fabio Viola, Brian Zhang, Ross Goroshin, Neil Rabinowitz, Razvan Pascanu, Charlie Beattie, Stig Petersen, Amir Sadik, Stephen Gaffney, Helen King, Koray Kavukcuoglu, Demis Hassabis, Raia Hadsell, and Dharshan Kumaran. Vector-based navigation using grid-like representations in artificial agents. *Nature*, 557(7705):429–433, May 2018.
- [25] Ben Sorscher, Gabriel C Mel, Surya Ganguli, and Samuel A Ocko. A unified theory for the origin of grid cells through the lens of pattern formation. *NeurIPS*, 2019.
- [26] Rylan Schaeffer, Mikail Khona, and Ila Rani Fiete. No Free Lunch from Deep Learning in Neuroscience: A Case Study through Models of the Entorhinal-Hippocampal Circuit, August 2022.
- [27] Rylan Schaeffer, Tzuhsuan Ma, Sanmi Koyejo, Mikail Khona, Cristóbal Eyzaguirre, and Ila Rani Fiete. Self-Supervised Learning of Representations for Space Generates Multi-Modular Grid Cells. *37th Conference on Neural Information Processing Systems (NeurIPS 2023)*, September 2023.
- [28] Amina A Kinkhabwala, Yi Gu, Dmitriy Aronov, and David W Tank. Visual cue-related activity of cells in the medial entorhinal cortex during navigation in virtual reality. *eLife*, 9:e43140, March 2020.
- [29] Duc Nguyen, Garret Wang, Talah Wafa, Tracy Fitzgerald, and Yi Gu. The medial entorhinal cortex encodes multisensory spatial information. *Cell Reports*, 43(10):114813, October 2024.
- [30] Qiming Shao, Ligu Chen, Xiaowan Li, Miao Li, Hui Cui, Xiaoyue Li, Xinran Zhao, Yuying Shi, Qiang Sun, Kaiyue Yan, and Guangfu Wang. A non-canonical visual cortical-entorhinal pathway contributes to spatial navigation. *Nature Communications*, 15(1):4122, May 2024.
- [31] Rajkumar Vasudeva Raju, J. Swaroop Guntupalli, Guangyao Zhou, Carter Wendelken, Miguel Lázaro-Gredilla, and Dileep George. Space is a latent sequence: A theory of the hippocampus. *Science Advances*, 10(31):eadm8470, August 2024.
- [32] Alexei Samsonovich and Bruce L. McNaughton. Path Integration and Cognitive Mapping in a Continuous Attractor Neural Network Model. *The Journal of Neuroscience*, 17(15):5900–5920, August 1997.
- [33] F. P. Battaglia and A. Treves. Attractor neural networks storing multiple space representations: A model for hippocampal place fields. *Physical Review E*, 58(6):7738–7753, December 1998.
- [34] Misha Tsodyks. Attractor neural network models of spatial maps in hippocampus. *Hippocampus*, 9(4):481–489, 1999.
- [35] E. T. Rolls. An attractor network in the hippocampus: Theory and neurophysiology. *Learning & Memory*, 14(11):714–731, November 2007.
- [36] Kimberly L Stachenfeld, Matthew M Botvinick, and Samuel J Gershman. The hippocampus as a predictive map. *Nature Neuroscience*, 20(11):1643–1653, November 2017.
- [37] Daniel Levenstein, Aleksei Efremov, Roy Henha Eyono, Adrien Peyrache, and Blake Richards. Sequential predictive learning is a unifying theory for hippocampal representation and replay, April 2024. bioRxiv.
- [38] Lila Davachi and Sarah DuBrow. How the hippocampus preserves order: The role of prediction and context. *Trends in Cognitive Sciences*, 19(2):92–99, February 2015.
- [39] Peter Kok and Nicholas B. Turk-Browne. Associative Prediction of Visual Shape in the Hippocampus. *The Journal of Neuroscience*, 38(31):6888–6899, August 2018.
- [40] John O’Keefe and Neil Burgess. Geometric determinants of the place fields of hippocampal neurons. *Nature*, 381(6581):425–428, May 1996.
- [41] Jared Deighton, Wyatt Mackey, Ioannis Schizas, David L. Boothe Jr, and Vasileios Maroulas. Higher-Order Spatial Information for Self-Supervised Place Cell Learning, June 2024.

- [42] George Dragoi and Susumu Tonegawa. Preplay of future place cell sequences by hippocampal cellular assemblies. *Nature*, 469(7330):397–401, January 2011.
- [43] H. Freyja Ólafsdóttir, Daniel Bush, and Caswell Barry. The Role of Hippocampal Replay in Memory and Planning. *Current Biology*, 28(1):R37–R50, January 2018.
- [44] Daniel Bush, Caswell Barry, Daniel Manson, and Neil Burgess. Using Grid Cells for Navigation. *Neuron*, 87(3):507–520, August 2015.
- [45] Taylor J. Malone, Nai-Wen Tien, Yan Ma, Lian Cui, Shangru Lyu, Garret Wang, Duc Nguyen, Kai Zhang, Maxym V. Myroshnychenko, Jean Tyan, Joshua A. Gordon, David A. Kupferschmidt, and Yi Gu. A consistent map in the medial entorhinal cortex supports spatial memory. *Nature Communications*, 15(1):1457, February 2024.
- [46] Jj Knierim, Hs Kudrimoti, and Bl McNaughton. Place cells, head direction cells, and the learning of landmark stability. *The Journal of Neuroscience*, 15(3):1648–1659, March 1995.
- [47] John O’Keefe and Julija Krupic. Do hippocampal pyramidal cells respond to nonspatial stimuli? *Physiological Reviews*, 101(3):1427–1456, July 2021.
- [48] Bruce L. McNaughton, Francesco P. Battaglia, Ole Jensen, Edvard I Moser, and May-Britt Moser. Path integration and the neural basis of the ‘cognitive map’. *Nature Reviews Neuroscience*, 7(8):663–678, August 2006.
- [49] I. R. Fiete, Y. Burak, and T. Brookings. What Grid Cells Convey about Rat Location. *Journal of Neuroscience*, 28(27):6858–6871, July 2008.
- [50] Dehong Xu, Ruiqi Gao, Wen-Hao Zhang, Xue-Xin Wei, and Ying Nian Wu. On Conformal Isometry of Grid Cells: Learning Distance-Preserving Position Embedding, February 2025.
- [51] Ru Muller and JI Kubie. The effects of changes in the environment on the spatial firing of hippocampal complex-spike cells. *The Journal of Neuroscience*, 7(7):1951–1968, July 1987.
- [52] Elizabeth Bostock, Robert U. Muller, and John L. Kubie. Experience-dependent modifications of hippocampal place cell firing. *Hippocampus*, 1(2):193–205, April 1991.
- [53] Philipp Schoenenberger, Joseph O’Neill, and Jozsef Csicsvari. Activity-dependent plasticity of hippocampal place maps. *Nature Communications*, 7(1):11824, June 2016.
- [54] Rosamund F. Langston, James A. Ainge, Jonathan J. Couey, Cathrin B. Canto, Tale L. Bjerknes, Menno P. Witter, Edvard I. Moser, and May-Britt Moser. Development of the Spatial Representation System in the Rat. *Science*, 328(5985):1576–1580, June 2010.
- [55] Tom J. Wills, Francesca Cacucci, Neil Burgess, and John O’Keefe. Development of the Hippocampal Cognitive Map in Preweanling Rats. *Science*, 328(5985):1573–1576, June 2010.
- [56] Tale L. Bjerknes, Nenitha C. Dagslott, Edvard I. Moser, and May-Britt Moser. Path integration in place cells of developing rats. *Proceedings of the National Academy of Sciences*, 115(7), February 2018.
- [57] Laurenz Muessig, Jonas Hauser, Thomas Joseph Wills, and Francesca Cacucci. A Developmental Switch in Place Cell Accuracy Coincides with Grid Cell Maturation. *Neuron*, 86(5):1167–1173, June 2015.
- [58] Caswell Barry, Lin Lin Ginzberg, John O’Keefe, and Neil Burgess. Grid cell firing patterns signal environmental novelty by expansion. *Proceedings of the National Academy of Sciences*, 109(43):17687–17692, October 2012.
- [59] Lisa M. Giocomo, Syed A. Hussaini, Fan Zheng, Eric R. Kandel, May-Britt Moser, and Edvard I. Moser. Grid Cells Use HCN1 Channels for Spatial Scaling. *Cell*, 147(5):1159–1170, November 2011.
- [60] Matthijs Douze, Alexandr Guzhva, Chengqi Deng, Jeff Johnson, Gergely Szilvasy, Pierre-Emmanuel Mazaré, Maria Lomeli, Lucas Hosseini, and Hervé Jégou. The faiss library. 2024.
- [61] Jeff Johnson, Matthijs Douze, and Hervé Jégou. Billion-scale similarity search with GPUs. *IEEE Transactions on Big Data*, 7(3):535–547, 2019.
- [62] Alexandra T Keinath, Russell A Epstein, and Vijay Balasubramanian. Environmental deformations dynamically shift the grid cell spatial metric. *eLife*, 7:e38169, October 2018.



- [63] Noga Mosheiff and Yoram Burak. Velocity coupling of grid cell modules enables stable embedding of a low dimensional variable in a high dimensional neural attractor. *eLife*, 8:e48494, August 2019.
- [64] Richard J. Gardner, Erik Hermansen, Marius Pachitariu, Yoram Burak, Nils A. Baas, Benjamin A. Dunn, May-Britt Moser, and Edvard I. Moser. Toroidal topology of population activity in grid cells. *Nature*, 602(7895):123–128, February 2022.
- [65] H Freyja Ólafsdóttir, Francis Carpenter, and Caswell Barry. Coordinated grid and place cell replay during rest. *Nature Neuroscience*, 19(6):792–794, June 2016.
- [66] J. O’Neill, C.N. Boccara, F. Stella, P. Schoenenberger, and J. Csicsvari. Superficial layers of the medial entorhinal cortex replay independently of the hippocampus. *Science*, 355(6321):184–188, January 2017.
- [67] J.J. Kuffner and S.M. LaValle. RRT-connect: An efficient approach to single-query path planning. In *Proceedings 2000 ICRA. Millennium Conference. IEEE International Conference on Robotics and Automation. Symposia Proceedings (Cat. No.00CH37065)*, volume 2, pages 995–1001, San Francisco, CA, USA, 2000. IEEE.
- [68] Gily Ginosar, Johnatan Aljadeff, Yoram Burak, Haim Sompolinsky, Liora Las, and Nachum Ulanovsky. Locally ordered representation of 3D space in the entorhinal cortex. *Nature*, 596(7872):404–409, August 2021.
- [69] Gily Ginosar, Johnatan Aljadeff, Liora Las, Dori Derdikman, and Nachum Ulanovsky. Are grid cells used for navigation? On local metrics, subjective spaces, and black holes. *Neuron*, 111(12):1858–1875, June 2023.
- [70] Sarthak Chandra, Sugandha Sharma, Rishidev Chaudhuri, and Ila Fiete. Episodic and associative memory from spatial scaffolds in the hippocampus. *Nature*, January 2025.
- [71] Trygve Solstad, Charlotte N. Boccara, Emilio Kropff, May-Britt Moser, and Edvard I. Moser. Representation of Geometric Borders in the Entorhinal Cortex. *Science*, 322(5909):1865–1868, December 2008.
- [72] Colin Lever, Stephen Burton, Ali Jeewajee, John O’Keefe, and Neil Burgess. Boundary Vector Cells in the Subiculum of the Hippocampal Formation. *The Journal of Neuroscience*, 29(31):9771–9777, August 2009.
- [73] Mark P. Brandon, Andrew R. Bogaard, Christopher P. Libby, Michael A. Connerney, Kishan Gupta, and Michael E. Hasselmo. Reduction of Theta Rhythm Dissociates Grid Cell Spatial Periodicity from Directional Tuning. *Science*, 332(6029):595–599, April 2011.
- [74] Geoffrey W. Diehl, Olivia J. Hon, Stefan Leutgeb, and Jill K. Leutgeb. Grid and Nongrid Cells in Medial Entorhinal Cortex Represent Spatial Location and Environmental Features with Complementary Coding Schemes. *Neuron*, 94(1):83–92.e6, April 2017.
- [75] James R. Hinman, Mark P. Brandon, Jason R. Climer, G. William Chapman, and Michael E. Hasselmo. Multiple Running Speed Signals in Medial Entorhinal Cortex. *Neuron*, 91(3):666–679, August 2016.
- [76] Jing Ye, Menno P. Witter, May-Britt Moser, and Edvard I. Moser. Entorhinal fast-spiking speed cells project to the hippocampus. *Proceedings of the National Academy of Sciences*, 115(7), February 2018.
- [77] Francesca Sargolini, Marianne Fyhn, Torkel Hafting, Bruce L. McNaughton, Menno P. Witter, May-Britt Moser, and Edvard I. Moser. Conjunctive Representation of Position, Direction, and Velocity in Entorhinal Cortex. *Science*, 312(5774):758–762, May 2006.

# 1 Supplementary Materials

## 1.1 Condition for Positivity of Prediction Error

Given two locations, the simplest navigation task can be framed as decoding the displacement vector between them from their corresponding grid cell representations. As suggested in Section 4.3, we propose that it is sufficient for navigation even if we first decode a displacement vector within each grid module and then combine them through simple averaging. Here, we examine what conditions are required to guarantee that the resulting averaged displacement always moves the animal closer to the target.

In the 1D case, or along one axis of a 2D case, the decoded displacement vector through simple averaging is given by:

$$\hat{d} = \frac{\ell_0}{2\pi m} \cdot \left( \sum_{i=1}^k s^i \cdot Z_i + \sum_{i=k+1}^m s^i \cdot \Delta\phi_i \right)$$

After taking this decoded displacement, the remaining distance to the target along the decoded direction is  $d - \hat{d}$ . To ensure the animal always moves closer to the target along this axis, it suffices to show that  $d - \hat{d} < d$ . Which is satisfied if  $m > k + \frac{1-s^{-k}}{s-1}$ .

*Proof.* Assume that all decodable scales yield the correct displacement vectors, i.e., for all  $i \in \{k+1, \dots, m\}$ , we have:

$$\frac{\ell_0 \cdot s^i \cdot \Delta\phi_i}{2\pi} = d$$

Substituting into the expression for  $\hat{d}$ :

$$d - \hat{d} = \frac{k}{m} \cdot d - \frac{\ell_0}{m \cdot 2\pi} \cdot \left( \sum_{i=1}^k s^i \cdot Z_i \right)$$

And thus we require

$$d - \hat{d} < d \quad \Leftrightarrow \quad (k - m) \cdot d < \frac{\ell_0}{2\pi} \cdot \left( \sum_{i=1}^k s^i \cdot Z_i \right)$$

Since that  $k$  is the index that delineates the decodable and undercovered scales,  $(\ell_0 \cdot s^k)/2 \leq d < (\ell_0 \cdot s^{k+1})/2$ . The worst case occurs when  $d$  takes its maximum value  $(\ell_0 \cdot s^{k+1})/2$  while  $Z_i$  takes its minimum value  $-\pi$ . Substituting these:

$$\begin{aligned} (k - m) \cdot \frac{\ell_0 \cdot s^{k+1}}{2} &< \frac{\ell_0}{2\pi} \cdot \left( \sum_{i=1}^k s^i \cdot (-\pi) \right) \\ \Rightarrow (k - m) \cdot s^{k+1} &< - \sum_{i=1}^k s^i = - \frac{s(s^k - 1)}{s - 1} \\ \Rightarrow k - m &< - \frac{s(s^k - 1)}{s^k s (s - 1)} = - \frac{1 - s^{-k}}{s - 1} \\ &\Rightarrow m > k + \frac{1 - s^{-k}}{s - 1} \end{aligned}$$

Notice that this bound only extend the initial assumption  $m > k$  by  $\frac{1-s^{-k}}{s-1}$  which never exceeds 1 when  $s = e$  for 1D case, and never exceeds 2 when  $s = \sqrt{e}$  for 2D space. Therefore, simple averaging reliably decreases the distance to the goal if  $m > k$  in 1D and  $m > k + 1$  in 2D.

□

## 2 Metrics

### 2.1 Spatial Information Content

We use spatial information content (SIC) [73] to measure the extent to which a cell might be a place cell. The SIC score quantifies how much knowing the neuron’s firing rate reduces uncertainty about the animal’s location. The SIC is calculated as

$$I = \sum_i^N p_i \cdot \frac{r_i}{\mathbb{E}[r]} \cdot \log_2 \left( \frac{r_i}{\mathbb{E}[r]} \right)$$

Where  $\mathbb{E}[r]$  is the mean firing rate of the cell,  $r_i$  is the firing rate at spatial bin  $i$ , and  $p_i$  is the empirical probability of the animal being in spatial bin  $i$ . For all cells with a mean firing rate above 0.01Hz, we discretize their firing ratemaps into 20 pixel  $\times$  20 pixel spatial bins and compute their SIC. We define a cell to be a place cell if its SIC exceeds 20.

## 3 Simulating Spatial Navigation Cells and Random Traversal Behaviors

### 3.1 Simulating Spatial Navigation Cells

In our model, we simulated the ground truth response of MEC cell types during navigation to supervise the training. We note that firing statistics for these cells vary significantly across species, environments, and experimental setups. Moreover, many experimental studies emphasize the phenomenology of these cell types rather than their precise firing rates. Thus, we simulate each type based on its observed phenomenology and scale its firing rate using the most commonly reported values in rodents. This scaling does not affect network robustness or alter the conclusions presented in the main paper. However, the relative magnitudes of different cell types can influence training dynamics. To mitigate this, we additionally employ a unitless loss function that ensures all supervised and partially supervised units are equally emphasized in the loss (see Suppl. 5.3.3).

**Spatial Modulated Cells:** We generate spatially modulated cells following the method in [16]. Notably, the simulated SMCs resemble the cue cells described in [28]. To construct them, we first generate Gaussian white noise across all locations in the environment. A 2D Gaussian filter is then applied to produce spatially smoothed firing rate maps.

Formally, let  $\mathcal{A} \subset \mathbb{R}^2$  denote the spatial environment, discretized into a grid of size  $W \times H$ . For each neuron  $i$  and location  $\mathbf{x} \in \mathcal{A}$ , the initial response is sampled as i.i.d. Gaussian white noise:  $\epsilon_i(\mathbf{x}) \sim \mathcal{N}(0, 1)$ . Each noise map  $\epsilon_i$  is then smoothed via 2D convolution with an isotropic Gaussian kernel  $G_{\sigma_i}$ , where  $\sigma_i$  represents the spatial tuning width of cell  $i$ . The raw cell response is then given by:

$$R_i^{\text{raw}} = \epsilon_i * G_{\sigma_i}$$

where  $*$  denotes the 2D convolution. The spatial width  $\sigma_i$  is sampled independently for each cell using  $\mathcal{N}(12\text{cm}, 3\text{cm})$ . Finally, the response of each cell is normalized using min-max normalization:

$$R_i = \frac{R_i^{\text{raw}} - \min(R_i^{\text{raw}})}{\max(R_i^{\text{raw}}) - \min(R_i^{\text{raw}})}$$

The SMCs used in our experiments model the sensory-related responses and non-grid cells in the MEC. Cue cells reported in [28] typically exhibit maximum firing rates ranging from 0–20Hz, but show lower firing rates at most locations distant from the cue. Non-grid cells reported in [74] generally have peak firing rates between 0–15Hz. To align with these experimental observations, we scale all simulated SMCs to have a maximum firing rate of 15Hz.

**Grid Cells:** To simulate grid cells, we generate each module independently. For a module with a given spatial scale  $\ell$ , we define two non-collinear basis vectors

$$\mathbf{b}_1 = \begin{bmatrix} \ell \\ 0 \end{bmatrix} \quad \text{and} \quad \mathbf{b}_2 = \begin{bmatrix} \ell/2 \\ \ell\sqrt{3}/2 \end{bmatrix}$$

These vectors generate a regular triangular lattice:

$$\mathcal{C} = \{n\mathbf{b}_1 + m\mathbf{b}_2 \mid n, m \in \mathbb{Z}\}$$

For each module, we randomly pick its relative orientation with respect to the spatial environment by selecting a random  $\theta \in [0, \pi/3)$  which is used to rotate the lattice:

$$\mathbf{R}^\theta = \begin{bmatrix} \cos \theta & -\sin \theta \\ \sin \theta & \cos \theta \end{bmatrix}, \quad \mathcal{C}_\theta = \{\mathbf{R}^\theta \mathbf{c} \mid \mathbf{c} \in \mathcal{C}\}$$

Within each module, individual cells are assigned unique spatial phase offsets. These offsets  $\psi_i$  are sampled from an equilateral triangle with vertices

$$V_1 = \mathbf{R}^\theta \begin{bmatrix} 0 \\ 0 \end{bmatrix} \quad V_2 = \mathbf{R}^\theta \begin{bmatrix} 0 \\ -\ell/2 \end{bmatrix} \quad V_3 = \mathbf{R}^\theta \begin{bmatrix} \ell\sqrt{3}/2 \\ -\ell/2 \end{bmatrix}.$$

We sample phase offsets for grid cells within each module by drawing vectors uniformly from the triangular region using the triangle reflection method. Since the resulting grid patterns are wrapped around the lattice, this is functionally equivalent to sampling uniformly from the full parallelogram. The firing centers for cell  $i$  in a given module are then given by:

$$\mathcal{C}_i = \{\mathbf{c}_i^* + \psi_i \mid \mathbf{c}_i^* \in \mathcal{C}_\theta\}$$

Finally, the raw firing rate map for cell  $i$  is generated by placing isotropic Gaussian bumps centered at each location in  $\mathcal{C}_i$ :

$$R_i^{\text{raw}} = \sum_{\mathbf{c}_i \in \mathcal{C}_i} \exp\left(-\frac{\|\mathbf{x} - \mathbf{c}_i\|^2}{2\sigma_{\text{grid}}^2}\right), \quad \mathbf{x} \in \mathcal{A}$$

where  $\sigma_{\text{grid}}$  is the spatial tuning width of each bump and is computed as:  $2\sigma_{\text{grid}} = \ell/r$  with  $r = 3.26$  following the grid spacing to field size ratio reported in [59]. Experimental studies have reported that rodent grid cells typically exhibit maximum firing rates in the range of 0–15Hz [7, 58], though most observed values are below 10Hz. Accordingly, we scale the generated grid cells to have a maximum firing rate of 10Hz.

**Speed Cells:** Many cells in the MEC respond to speed, including grid cells, head direction cells, conjunctive cells, and uncategorized cells [75, 76]. These cells may show saturating, non-monotonic, or even negatively correlated responses to movement speed. To maintain simplicity in our model, we represent speed cells as units that respond exclusively and linearly to the animal’s movement speed. Specifically, we simulate these cells with a linear firing rate tuning based on the norm of the displacement vector  $\vec{d}$  at each time step, which reflects the animal’s instantaneous speed.

Additionally, many reported speed cells exhibit high baseline firing rates [75, 76]. To avoid introducing an additional parameter, we set all speed cells’ tuning to start from zero—i.e., their firing rate is 0Hz when the animal is stationary. To introduce variability across cells, each speed cell is assigned a scaling factor  $s_i$  sampled from  $\mathcal{N}(0.2, 0.05)$  Hz/(cm/s), allowing cells to fire at different rates for the same speed input. Given that the simulated agent has a mean speed of 10cm/s (Suppl. 3.2), the average firing rate of speed cells is approximately 2Hz. We chose a lower mean firing rate than observed in rodents, as we did not include a base firing rate for the speed cells. However, this scaling allows cells with the strongest speed tuning to reach firing rates up to 80Hz, matching the peak rates reported in [76] when the agent moves at its fastest speed.

All cells follow the same linear speed tuning function:

$$R_i(\vec{d}) = \frac{s_i \cdot \|\vec{d}\|}{dt}$$

where  $dt$  is the simulation time resolution (in seconds),  $\|\vec{d}\|$  is the displacement magnitude over that interval, and  $s_i$  modulates the response sensitivity of each cell.

**Direction Cells:** We define direction cells based on the movement direction of the animal, rather than its body or head orientation. During initialization, each cell is assigned a preferred allocentric direction drawn uniformly at random from the interval  $[0, 2\pi)$ . At any time during the animal’s movement, we extract its absolute displacement vector  $\vec{d}$ . From this vector, we compute the angular difference  $\Delta\theta$  between the allocentric movement direction and the  $i$ -th cell’s preferred direction. The movement direction can be derived from the displacement vector  $\vec{d}$ . Each neuron responds according to a wrapped Gaussian tuning curve:

$$R_i(\theta) = \exp\left(-\frac{[\Delta\theta_i]_{2\pi}^2}{2\sigma_{\text{dir}}^2}\right)$$

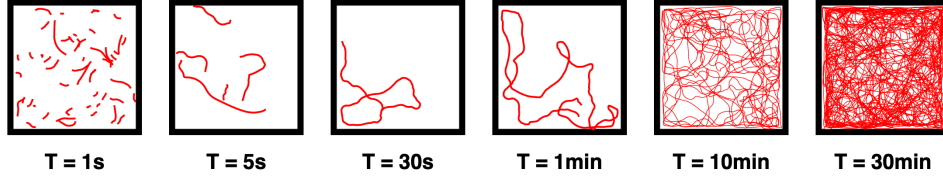


**Figure S1:** Example generated trajectories of varying lengths. From left to right: 50 trajectories of 1s each, 5 trajectories of 5s, followed by single trajectories of 30s, 1min, 10min, and 30min.

where  $[\Delta\theta_i]_{2\pi}$  denotes the angular difference wrapped into the interval  $[0, 2\pi)$ .  $\sigma_{\text{dir}}$  denotes the tuning width (standard deviation) of the angular response curve. We set  $\sigma_{\text{dir}} = 1$  rad to reduce the number of direction cells needed to span the full angular space  $[0, 2\pi)$ , thereby decreasing the size of the RNN to improve training efficiency. Given that many head direction cells in the MEC are conjunctive with grid and speed cells [77], we set the mean firing rate of direction cells to 2Hz to match the typical firing rates of speed cells.

We acknowledge that this simulation of the direction cell may only serve as a simplified model. However, in our model, direction cells serve only to provide input to grid cells for path integration, and we have verified that the precise tuning width and magnitude do not affect the planning performance or change the conclusion of the main text. Our findings could be further validated by future studies employing more biologically realistic simulation methods.

### 3.2 Simulating Random Traversal Behaviors

We train our HC-MEC model using simulated trajectories of random traversal, during which we sample masked observations of displacement and sensory input. The network is trained to reconstruct the unmasked values of speed, direction, SMC, and grid cell responses at all timepoints. Trajectories are simulated within a  $100 \times 100\text{cm}^2$  arena, discretized at 1 cm resolution per spatial bin. The agent’s movement is designed to approximate realistic rodent behavior by incorporating random traversal with momentum.

At each timestep, the simulated agent’s displacement vector  $\vec{d}$  is determined by its current velocity magnitude, movement direction, and a stochastic drift component. The base velocity  $v$  is sampled from a log-normal distribution with mean  $\mu_{\text{spd}} = 10$  and standard deviation  $\sigma_{\text{spd}} = 10$  (in cm/s), such that the agent spends most of its time moving below 10 cm/s but can reach up to 50 cm/s. The velocity is converted to displacement by dividing by the simulation time resolution  $dt$ , and re-sampled at each timestep with a small probability  $p_{\text{spd}}$  to introduce variability.

To simulate movement with momentum, we add a drift component that perturbs the agent’s displacement. The drift vector is computed by sampling a random direction, scaling it by the current velocity and a drift coefficient  $c_{\text{drift}}$  that determines the drifting speed. Drift direction is resampled at each step with a small probability  $p_{\text{dir}}$  to simulate the animal switch their traversal direction. The drift is added to the direction-based displacement, allowing the agent to move in directions slightly offset from its previous heading. This results in smooth trajectories that preserve recent movement while enabling gradual turns.

To prevent frequent collisions with the environment boundary, a soft boundary-avoidance mechanism is applied. When the agent is within  $d_{\text{avoid}}$  pixels of a wall and its perpendicular distance to the wall is decreasing, an angular adjustment is applied to its direction. This correction is proportional to proximity and only engages when the agent is actively moving toward the wall. We set  $dt = 0.01$  sec/timestep,  $p_{\text{spd}} = 0.02$ ,  $c_{\text{drift}} = 0.05$ ,  $p_{\text{dir}} = 0.15$ , and  $d_{\text{avoid}} = 10$  pixels. These values were chosen to produce trajectories that qualitatively match rodent traversal (see Fig S1).

## 4 Decoding Location from Population Activity

In the main text, we decode the population vector to locations in both the recall task (Section 3) and the planning task (Section 4.4). Here we present the method we used for such decoding. Given a population vector  $\mathbf{r} \in \mathbb{R}^N$  at a given timestep, we decode it into a location estimate by performing nearest neighbor search over a set of rate maps corresponding to the subpopulation of



cells corresponding to  $\mathbf{r}$ . These rate maps may come from our simulated ground-truth responses or be aggregated from the network’s activity during testing (see Suppl. 5.4).

Formally, let  $\mathbf{r} = [r_1, r_2, \dots, r_N]$  be the population response of a subpopulation of  $N$  cells at a given timestep, and let  $M \in \mathbb{R}^{P \times N}$  be the flattened rate maps, where each row  $m_p$  corresponds to the population response at the  $p$ -th spatial bin. Here,  $P = W \times H$  is the total number of discretized spatial bins in the environment  $\mathcal{A}$ . The decoding process is to find the index  $p^*$  that minimizes the Euclidean distance between  $\mathbf{r}$  and  $m_p$ :

$$p^* = \arg \min_p \|\mathbf{r} - m_p\|_2$$

To efficiently implement this decoding, we use the FAISS library [60, 61]. Specifically, we employ the `IndexIVFFlat` structure, which first clusters the rows  $\{m_p\}_{p=1}^P$  into  $k$  clusters using  $k$ -means. Each vector  $m_p$  is then assigned to its nearest centroid, creating an inverted index that maps each cluster to the set of vectors it contains.

At query time, the input vector  $\mathbf{r}$  is first compared to all centroids to find the `n_probe` closest clusters. The search is then restricted to the vectors assigned to these clusters. Finally, the nearest neighbor among them is returned, and its index  $p^*$  is mapped back to the corresponding spatial coordinate  $\mathbf{x}^*$ . For all experiments, we set the `n_clusters` for the  $k$ -means to 100 and `n_probe` to 10.

## 5 Training and Testing of the HC-MEC Model

As described in Section 2.1, our HC-MEC model is a single-layer RNN composed of multiple sub-networks. We train two versions of this model: (1) **GC-only** variant, which includes only grid cells and along with speed and direction cells; and (2) the full **HC-MEC** loop model, which includes both MEC and hippocampal (HC) subpopulations.

In both cases, we simulate ground-truth responses for supervised and partially supervised cells using the method described in Suppl. 3. The number of simulated cells matches exactly the number of corresponding units in the RNN hidden layer. That is, if we simulate  $N_g$  grid cells, we assign precisely  $N_g$  hidden units in the RNN to represent them, and (partially)-supervise these units with the corresponding ground-truth activity. Additional details on this partial supervision are provided in Suppl. 5.1.

For both models, we use six scales of grid cells, with the initial spatial scale set to 30cm. Subsequent scales follow the theoretically optimal scaling factor  $s = \sqrt{e}$  [12]. The grid spacing to field size ratio is fixed at 3.26 [59]. Each scale comprises 48 grid cells, and the spatial phase offsets for each cell within a module are independently sampled from the corresponding equilateral triangle (Suppl. 3) with side length equals to the spatial scale of the module. In addition, both the **GC-only** and **HC-MEC** models include 32 speed cells and 32 direction cells.

The **HC-MEC** model additionally includes spatially modulated cells (SMCs) in the MEC subpopulation and hippocampal place cells (HPCs) in the HC subpopulation. We include 256 SMCs to approximately match the number of grid cells. These SMCs are designed to reflect responses to sensory experience and are trained with supervision as described in Suppl. 3. We also include 512 HPCs, matching approximately the total number of grid cells and SMCs ( $N = 256 + 288$ ). These cells only receive input from and project to the MEC subpopulation through recurrent connections, and thus do not receive any external input. We note that, differing from [16], we did not apply a firing rate constraint on the HPCs, but still observed the emergence of place cell-like responses.

In total, unless otherwise specified, our **GC-only** model comprises 352 hidden units ( $48 \times 6$  grid cells + 32 speed cells + 32 direction cells), while the **HC-MEC** model comprises 1120 hidden units (288 grid cells + 32 speed cells + 32 direction cells + 256 SMCs + 512 HPCs).

### 5.1 Supervising Grid Cells

As described in Section 2.1, we partially supervise the grid cell subpopulation of the RNN using simulated ground-truth responses. Let  $\mathbf{z}_t \in \mathbb{R}^{N_g}$  denote the hidden state of the RNN units modeling grid cells at time  $t$ . During training, the HC-MEC model is trained on short random traversal trajectories. Along each trajectory, we sample the ground-truth grid cell responses from the simulated ratemaps at the corresponding location and denote these as  $\{\mathbf{r}_t^g\}_{t=0}^T$ . At the start of each trajectory, we initialize the grid cell units with the ground-truth response at the starting location, i.e.,  $\mathbf{z}_0 = \mathbf{r}_0^g$ .

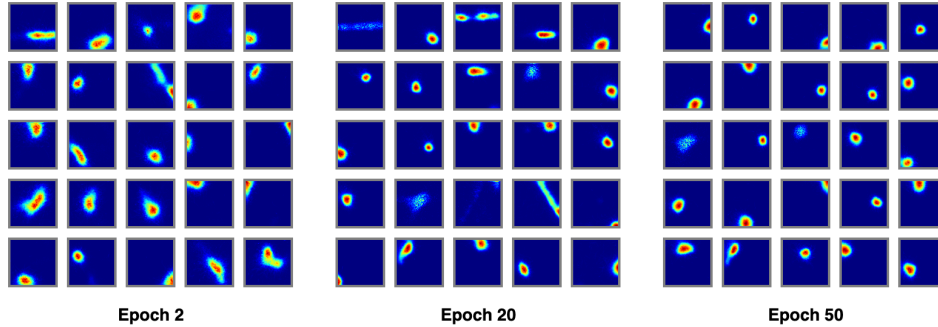


**Figure S2:** Example place fields emerging over training. Shown are place fields from epoch 2, 20, and 50. As training progresses, the fields become increasingly specific and spatially refined.

From time step  $t = 1$  to  $T$ , the grid cell hidden states  $\mathbf{z}_t$  are updated solely through recurrent projections between the grid cell subpopulation and the speed and direction cells. They do not receive any external inputs. After the RNN processes the speed and direction inputs over the entire trajectory, we collect the hidden states of the grid cell subpopulation  $\{\mathbf{z}_t\}_{t=1}^T$  and minimize their deviation from the corresponding ground-truth responses  $\{\mathbf{r}_t^g\}_{t=1}^T$ . The training loss function is described in Suppl. 5.3.3.

We choose to partially supervise the grid cells due to their critical role in the subsequent training of the planning network. This supervision allows the model to learn stable grid cell patterns, reducing the risk of instability propagating into later stages of training. While this partial supervision does not reflect fully unsupervised emergence, it can still be interpreted as a biologically plausible scenario in which grid cells and place cells iteratively refine each other’s representations. Experimentally, place cell firing fields appear before grid cells but become more spatially specific as grid cell patterns stabilize, potentially due to feedforward projections from grid cells to place cells [56, 57].

We observe a similar phenomenon during training. Even with partial supervision, grid cells tend to emerge after place cells. This may be because auto-associating spatially modulated sensory representations is easier than learning the more structured path-integration task hypothesized to be performed by grid cells. After the grid cells’ pattern stabilizes, we also observe that place cell firing fields become more refined (Fig. S2), consistent with experimental findings [3, 54–56].

## 5.2 HC-MEC Training Task

During navigation, animals may use two different types of sensory information to help localize themselves: (1) sensory input from the environment to directly observe their location; and (2) displacement information from the previous location to infer the current location and potentially reconstruct the expected sensory observation. We posit that the first type of information is reflected by the weakly spatially modulated cells (SMCs) in the MEC, while the second type is reflected by grid cells and emerges through path integration.

However, as we previously argued in Section 2.1, both types of information are subject to failure during navigation. Decades of research have revealed the strong pattern completion capabilities of hippocampal place cells. We thus hypothesize that hippocampal place cells may help reconstruct one type of representation from the other through auto-associative mechanisms.

To test this hypothesis, we simulate random traversal trajectories and train our **HC-MEC** model with masked sensory inputs. The network is tasked with reconstructing the ground-truth responses of all MEC subpopulations from simulation, given only the masked sensory input along the trajectory. Specifically, the supervised units—SMCs, speed cells, and direction cells—receive masked inputs to simulate noisy sensory perception. We additionally mask the ground-truth responses used to initialize both supervised and partially supervised units at  $t = 0$ , so that the network dynamics also begin from imperfect internal states.

To simulate partial or noisy observations, we apply masking on a per-trajectory and per-cell basis. For a given trajectory, we sample the ground-truth responses along the path to form a matrix

$\mathbf{R} = [\mathbf{r}_0 \cdots \mathbf{r}_T]^\top \in \mathbb{R}^{T \times N}$ , where  $N$  is the number of cells in the sampled subpopulation and  $\mathbf{r}_t$  is the ground-truth population response at time  $t$ . The masking ratio  $r_{\text{mask}}$  defines the maximum fraction of sensory and movement-related inputs, as well as initial hidden states, that are randomly zeroed during training to simulate partial or degraded observations. We generate a binary mask  $\mathbf{M} \in \{0, 1\}^{T \times N}$  by thresholding a matrix of random values drawn uniformly from  $[0, 1]$ , such that approximately  $100 \times r_{\text{mask}}$  percent of the entries are set to zero. The final masked response is then obtained by elementwise multiplication  $\tilde{\mathbf{R}} = \mathbf{R} \odot \mathbf{M}$ .

During training, we sample multiple trajectories to form a batch, with each trajectory potentially having a different masking ratio and masked positions. For both the HC-MEC model used in the recall task (Section 2) and the one pre-trained for the planning task (Section 4.4), masking ratios for SMCs and other inputs are sampled independently from the interval  $[0, r_{\text{mask}}]$ . Specifically, for each trial, we sample:

$$m_{\text{SMC}}, m_{\text{other}} \sim \mathcal{U}(0, r_{\text{mask}})$$

We use  $m_{\text{SMC}}$  to generate the mask for SMC cells, and  $m_{\text{other}}$  to independently generate masks for grid cells, speed cells, and direction cells. This allows the model to encounter a wide range of noise conditions during training—for example, scenarios where sensory inputs are unreliable but displacement-related cues are available, and vice versa.

### 5.3 RNN Implementation

#### 5.3.1 Initialization

Our HC-MEC model includes multiple sub-regions. However, we aim to model these sub-regions without imposing explicit assumptions about their connectivity, as the precise connectivity—particularly the functional connectivity between the hippocampus (HC) and medial entorhinal cortex (MEC)—remains unknown. Modeling these sub-regions with multiple hidden layers would implicitly enforce a unidirectional flow of information: the second layer would receive input from the first but would not project back. Specifically, a multi-layer RNN with two recurrent layers can be represented by a block-structured recurrent weight matrix:

$$\mathbf{W} = \begin{bmatrix} \mathbf{W}^{11} & \mathbf{W}^{12} \\ \mathbf{W}^{21} & \mathbf{W}^{22} \end{bmatrix}$$

Where  $\mathbf{W}^{11}$  and  $\mathbf{W}^{22}$  are the recurrent weight matrices of the first and second recurrent layers, respectively, and  $\mathbf{W}^{12}$  is the projection weights from the first to the second layer. In typical multi-layer RNN setups,  $\mathbf{W}^{12} = \mathbf{0}$ , meaning that the second sub-region does not send information back to the first. This structure generalizes to deeper RNNs, where only the diagonal blocks  $\mathbf{W}^{ii}$  and the blocks directly below the diagonal  $\mathbf{W}^{(i+1)i}$  are non-zero.

Therefore, we model the HC-MEC system as a large single-layer RNN, such that all sub-blocks are initialized as non-zero, and their precise connectivity is learned during training and entirely defined by the task. To initialize this block-structured weight matrix, we first initialize each subregion independently as a single-layer RNN with a defined weight matrix but no active dynamics. Suppose we are modeling  $N_r$  subregions, and each subregion  $i$  contains  $d_i$  hidden units. We initialize the recurrent weights within each subregion using a uniform distribution:

$$\mathbf{W}^{ii} \sim \mathcal{U}(-1/\sqrt{d_i}, 1/\sqrt{d_i})$$

For each off-diagonal block  $\mathbf{W}^{ij}$ , corresponding to projections from subregion  $j$  to subregion  $i$ , we similarly initialize:

$$\mathbf{W}^{ij} \sim \mathcal{U}(-1/\sqrt{d_j}, 1/\sqrt{d_j})$$

Note that the initialization bound is determined by the size of the source subregion  $j$ , consistent with standard practices for stabilizing the variance of the incoming signals. Once initialized, all sub-blocks are copied into their respective locations within a full recurrent weight matrix:

$$\mathbf{W}_{\text{HCMEC}} = \begin{bmatrix} \mathbf{W}^{11} & \cdots & \mathbf{W}^{1N} \\ \vdots & \ddots & \vdots \\ \mathbf{W}^{N_r,1} & \cdots & \mathbf{W}^{N_r,N_r} \end{bmatrix}$$

with total size  $\sum_{i=1}^{N_r} d_i \times \sum_{i=1}^{N_r} d_i$ .

Additionally, as described in main text, both input and output neurons are already modeled within the HC-MEC model. As a result, no additional input or output projections are required. Input neurons in this assembled RNN directly integrate external signals from the simulation, while the states of output neurons are directly probed out during training.

### 5.3.2 Parameters

For models used in the recall and planning tasks, we use the following parameters:

**Table 1:** Shared parameters for **GC-only** and **HC-MEC** models

Parameter	Value	Description
$N_{\text{speed}}$	32	Number of speed cells
$N_{\text{direction}}$	32	Number of direction cells
$N_{\text{grid}}$ (per module)	48	Number of grid cells per module
n_modules	6	Number of spatial scales (modules)
initial_scale	30 cm	Spatial period of the smallest module
spatial_scale_factor	$\sqrt{e}$	Scale ratio between adjacent modules
$r_{\text{grid/field}}$	3.26	Grid spacing to field size ratio
activation	ReLU	Activation function of the hidden units
$dt$	0.05 s	Time res for both cell simulation and RNN, 1s = 20 bins
$\alpha_{\text{init}}$	0.2	Initial forgetting rate of the cells
learn_alpha	True	Whether the forgetting rate is learned during training
optimizer	AdamW	Optimizer
learning_rate	0.001	Learning rate
batch_size	128	Batch size, each batch corresponds to a single trajectory
n_epochs	50	Number of training epochs
n_steps	1000	Number of steps per trajectory
$T_{\text{trajectory}}$	2 s	Duration of each training trajectory

In Section 4.4 of the main text, we noted that the **GC-Only** model used for planning uses  $N_{\text{grid}} = 128$ , i.e., each module comprised 128 grid cells. This larger population improves planning accuracy, likely due to denser coverage of the space. However, for the full **HC-MEC** model used in planning, we reverted to  $N_{\text{grid}} = 48$ , consistent with our default configuration. As discussed in the main text, the auto-associative dynamics from place cells help smooth the trajectory, even when the decoded trajectory from grid cells is imperfect.

**Table 2:** Additional parameters for **HC-MEC** model

Parameter	Value	Description
$N_{\text{SMC}}$	256	Number of spatially modulated cells
$\sigma_{\text{SMC}}$	$\mathcal{N}(12\text{cm}, 3\text{cm})$	Width of Gaussian smoothing to generate SMCs, which controls the spatial sensitivity of SMCs (see Suppl. 3)
$N_{\text{HPC}}$	512	Number of hippocampal place cells

### 5.3.3 Loss Function

We use a unitless MSE loss for all supervised and partially supervised units such that all supervised cell types are equally emphasized. For each trajectory, we generate ground-truth responses by sampling the corresponding region’s simulated ratemaps at the trajectory’s locations, resulting in  $\{\mathbf{r}_t\}_{t=0}^T$ . After the RNN processes the full trajectory, we extract the hidden states of the relevant units to obtain  $\{\mathbf{z}_t\}_{t=0}^T$ . To ensure that all loss terms are optimized equally and are not influenced by the scale or variability of individual cells, we perform per-cell normalization of the responses. For each region  $i$ , we compute the mean  $\boldsymbol{\mu}^i \in \mathbb{R}^{d_i}$  and standard deviation  $\boldsymbol{\sigma}^i \in \mathbb{R}^{d_i}$  of the ground-truth responses across the time and batch dimensions, independently for each cell. The responses are then normalized

elementwise:

$$\hat{\mathbf{r}}_t^i = \frac{\mathbf{r}_t^i - \boldsymbol{\mu}^i}{\boldsymbol{\sigma}^i}, \quad \hat{\mathbf{z}}_t^i = \frac{\mathbf{z}_t^i - \boldsymbol{\mu}^i}{\boldsymbol{\sigma}^i}$$

The total loss across all regions is computed as the mean squared error between the normalized responses:

$$\mathcal{L} = \frac{1}{T} \sum_{i=1}^{N_r} \sum_{t=1}^T \lambda_i \|\hat{\mathbf{z}}_t^i - \hat{\mathbf{r}}_t^i\|_2^2$$

where  $\lambda$  controls the relative weights of each cell types. We set the  $\lambda = 10$  for both grid cells and SMCs, while  $\lambda = 1$  for velocity and direction cells. These relative weights are set as animals may emphasize their reconstruction of the sensory experience and relative location, rather than their precise speed and direction during their spatial traversal.

#### 5.4 Constructing Ratemaps During Testing

After training, we test the agent using a procedure similar to training to estimate the firing statistics of hidden units at different spatial locations and construct their ratemaps. Specifically, we pause weight updates and generate random traversal trajectories. The supervised and partially supervised units are initialized with masked ground-truth responses, and the supervised units continue to receive masked ground-truth inputs at each timestep. We record the hidden unit activity of the RNN at every timestep and aggregate their average activity at each spatial location.

Let  $\mathbf{z}_t \in \mathbb{R}^d$  be the hidden state or a subpopulation of hidden states of the RNN at time  $t$ , where  $d$  is the number of hidden units. For each unit  $i$ , the ratemap value at location  $\mathbf{x}$  is computed as:

$$R_i(\mathbf{x}) = \begin{cases} \frac{1}{N(\mathbf{x})} \sum_{t:\mathbf{x}_t=\mathbf{x}} \mathbf{z}_t^i & \text{if } N(\mathbf{x}) > 0 \\ \text{NaN} & \text{otherwise} \end{cases}$$

where  $N(\mathbf{x})$  is the number of times location  $\mathbf{x}$  was visited during testing. We set the trajectory length to  $T = 5\text{s}$  (250 time steps), `batch_size` = 512, and `n_batches` = 200. We perform this extensive testing to ensure that the firing statistics of all units are well estimated. Each spatial location is visited on average  $1008.13 \pm 268.24$  times (mean  $\pm$  standard deviation).

## 6 Recall Task

In this paper, we have posited that the auto-association of place cells may trigger the reconstruction of grid cell representations given sensory observations. To test whether such reconstruction is possible, we trained nine different models, each with a fixed masking ratio  $r_{\text{mask}}$  ( $m_r$  in the main text) ranging from 0.1 to 0.9. Following the procedure described in Suppl. 5.2, each model was trained with the same masking ratio applied to all subregions and across all trials, but the masking positions were generated independently for each trial. That is, for each trial,  $100 \times r_{\text{mask}}$  of the entries were occluded. The mask was applied both to the ground-truth responses used to initialize the network and to the subsequent inputs.

After training, we tested recall by randomly selecting a position in the arena and sampling the ground-truth response of the SMC subpopulation to represent the sensory cues. This sampled response was then repeated over  $T = 10\text{s}$  (200 time steps) to form a constant input query. Unlike training, the initial state of the network was set to zero across all units, such that the network dynamics evolved solely based on the queried sensory input.